

University of Winnipeg

All-optical Atomic Magnetometry using Nonlinear Magneto-optical  
Effects

by

Cameron Cerasani

A thesis submitted in fulfillment of the requirements for the degree of

Bachelor of Science, Honours

Department of Physics

© Cameron Cerasani  
Spring 2014  
Winnipeg, Manitoba

# Abstract

All-optical Atomic Magnetometry using Nonlinear Magneto-optical Effects

Cameron Cerasani

B.Sc. Honours

Department of Physics

University of Winnipeg

2014

Improvements were made to the existing rubidium atomic magnetometer which uses nonlinear magneto-optical rotation. Magnetic properties of the system were studied and are discussed in detail, including shielding, mapping, degaussing, sweep rate, and off axis fields. Laser parameters were also optimized, including beam intensity and frequency detuning, to determine the optimal settings for this system. An apparatus was developed to quantify the relaxation time of vapour cells, and ultimately determined that cell quality is the most important parameter presently limiting magnetometer performance, with 100 times further improvement possible in the future. The narrowest resonance width observed on the  $D_1$ ,  $^{85}\text{Rb}$   $F = 3 \rightarrow F = 2,3$  resonance was  $130 \mu\text{G}$  with a light intensity of  $\sim 38 \mu\text{W}$ . Bandwidth limitations on our non zero amplitude modulated nonlinear magneto-optical rotation system were diagnosed and systematically removed so that operation is possible at frequencies of 100 kHz corresponding to fields of 100 mG. The precision of the magnetometer is presently  $\sim 25 \text{ nG}$  for quasi-DC fields, again limited by cell quality.

# Contents

<b>1</b>	<b>Introduction to NMOR</b>	<b>2</b>
1.1	Motivation . . . . .	2
1.2	Previous Work . . . . .	4
1.3	Systematic Improvements . . . . .	5
<b>2</b>	<b>Theory</b>	<b>6</b>
2.1	Linear Faraday Rotation . . . . .	6
2.2	NMOR . . . . .	7
2.3	AM NMOR . . . . .	9
2.4	Relaxation Time . . . . .	10
<b>3</b>	<b>Experimental Set Up</b>	<b>12</b>
3.1	Laser . . . . .	12
3.2	NMOR at Zero Field . . . . .	12
3.3	NMOR at Non-zero Field . . . . .	14
3.4	Magnetic Shielding . . . . .	14
3.5	Internal Coil . . . . .	16
3.6	Relaxation Time . . . . .	17
<b>4</b>	<b>Analysis</b>	<b>20</b>
4.1	NMOR near Zero Field . . . . .	20
4.1.1	Fit Analysis . . . . .	21
4.1.2	Magnetic Parameters . . . . .	21

4.1.3	Laser Parameters . . . . .	26
4.1.4	Cell Quality . . . . .	29
4.2	NMOR at Non Zero Field . . . . .	31
4.3	Magnetometry . . . . .	34
<b>5</b>	<b>Summary</b>	<b>37</b>
5.1	Results . . . . .	37
5.2	Future Work . . . . .	38

# List of Figures

1.1	D. Budker's NMOR . . . . .	4
2.1	Atomic splitting of the ground state . . . . .	7
2.2	Linear vs. nonlinear optical rotation . . . . .	9
2.3	Relaxation time of Balabas' cell . . . . .	11
3.1	NMOR apparatus . . . . .	13
3.2	AM NMOR apparatus . . . . .	15
3.3	Old and new magnetic shield comparison . . . . .	16
3.4	New magnetic shield maps . . . . .	17
3.5	New coil . . . . .	18
3.6	Coil schematic . . . . .	18
3.7	Old and new coil calibration . . . . .	19
3.8	Relaxation time apparatus . . . . .	19
4.1	NMOR width progression . . . . .	21
4.2	Pre and post degaussing . . . . .	23
4.3	Off axis magnetic fields . . . . .	24
4.4	Optical rotation with magnetic sweep rate dependence . . . . .	26
4.5	NMOR width versus light intensity . . . . .	27
4.6	Frequency detuning . . . . .	28
4.7	NMOR before and after heat gunning the cell . . . . .	30
4.8	Relaxation time measurement . . . . .	31

4.9	D. Budker's vapour cell . . . . .	32
4.10	Photodiodes . . . . .	33
4.11	AOM response time . . . . .	34
4.12	Magnetometer at 48 nG . . . . .	35
4.13	Magnetometer at 25 nG . . . . .	36
4.14	Magnetometer at 10 nG . . . . .	36

# Chapter 1

## Introduction to NMOR

Linear magneto-optical rotation, also known as Faraday rotation or the Faraday effect, was first discovered in the mid 1800's. Faraday rotation describes the interaction and rotation of the plane of polarization of light in a medium about an axial magnetic field. Nonlinear effects arise when properties of the medium are modified by the incident light. Near an atomic resonance, rotation can be enhanced in the presence of a magnetic field. This makes nonlinear magneto-optical rotation (NMOR) based magnetometers some of the most sensitive magnetometers available. Such magnetometers are applicable to a variety of fields including geology, biology, fundamental physics, space science, and other fields requiring high sensitivity magnetometry [1].

### 1.1 Motivation

The end goal of this research is to produce an all-optical magnetometer for the neutron electric dipole moment (nEDM) experiment capable of  $<1$  nG sensitivity. All-optical magnetometry based on NMOR addresses several limitations of magnetometers available commercially.

One type of magnetometer is a fluxgate magnetometer. Fluxgate magnetometers operate using magnetic cores which are driven in and out of saturation around

a hysteresis loop. This means they strongly perturb the surrounding magnetic environment. Furthermore, they have a limited sensitivity of 100 nG [2].

Another type of magnetometer is a Superconducting Quantum Interference Device (SQUID). These magnetometers rely on the superconducting property of trapped magnetic flux. Because of this, they must be operated at cryogenic temperatures. SQUID magnetometers are sensitive to the 0.01 nG level [3], but keeping a device at extremely low temperatures would be impractical for the nEDM experiment. Spin Exchange Relaxation-Free (SERF) magnetometers boast greater sensitivity than SQUID magnetometers with SERF magnetic sensitivity reaching the 10 fG level [3]. Their limited dynamic range is problematic for non-zero measurements.

The most similar in sensitivity to NMOR magnetometers are radio frequency (RF) atomic magnetometers, or MX magnetometers [4]. With nG sensitivity and the same basic principles as all-optical, they are an attractive option. A drawback is that the alignment of the atoms crucial to atomic magnetometry are achieved using radio frequency magnetic fields, which again perturb the magnetic environment, however only at high frequency.

All-optical atomic magnetometers provide a viable solution in combining the perks of each of the previous devices. Since they are all-optical, the atoms are aligned using light, eliminating the noise caused by radio frequencies. Further, optimized systems are capable of achieving sensitivity in the SQUID range [5], but without the cost and practicality of superconductors. All-optical magnetometers also have advantageous quality of being able to operate remotely. As long as there is a laser and a vapour cell, you can achieve high sensitivity magnetometry. These qualities are all beneficial to the nEDM experiment.

## 1.2 Previous Work

Though Faraday rotation was discovered over two centuries ago, recent advancements in technology related to NMOR have revitalized interest in the field. Measurements using amplitude/frequency modulated (AM/FM) light have demonstrated 3 nG sensitivity in Earth's magnetic field [1]. Applying NMOR to prac-

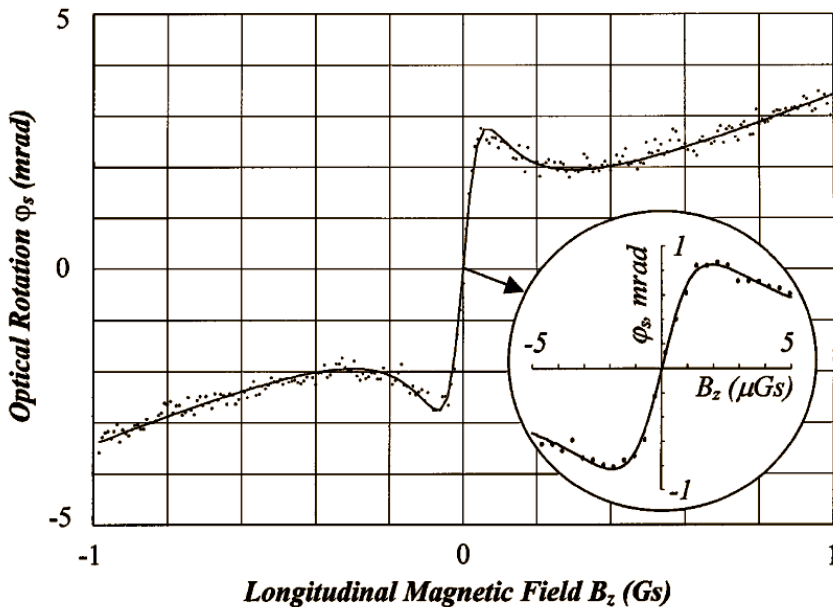


Figure 1.1: Optical rotation dependence on field strength from [6]. Laser tuned near the  $D_2$   $F = 3$  transition of  $^{85}\text{Rb}$ . The narrow feature width at zero field with a valley at  $-1.4 \mu\text{G}$  and peak at  $1.4 \mu\text{G}$  (inset) is indication of a nonlinear effect.

tical all-optical magnetometry is dependent on the width of the optical rotation feature shown in Fig. 1.1. The width of the feature is the nonlinear effect at zero field with a valley at  $-1.4 \mu\text{G}$  and peak at  $1.4 \mu\text{G}$ . Narrower widths yield higher sensitivity magnetometers. To date, the narrowest width published is  $2.8 \mu\text{G}$  [6].

NMOR widths are directly related to the relaxation time of the ground state polarization  $\gamma_{rel}$  (longer relaxation time  $\rightarrow$  narrow widths), thus motivating the need for high quality paraffin coated cells. These high quality cells have relaxation times of order seconds. A system designed to measure relaxation time was developed and tested following a similar method as described in [7]. This allowed

us to quantify the quality of our cells.

### 1.3 Systematic Improvements

The goal of this work was to understand and improve the existing Rb NMOR system at the University of Winnipeg, with the intent of developing a highly sensitive all-optical magnetometer for the nEDM experiment. The existing system was studied extensively and system parameters were tested and calibrated experimentally.

The principle system variables studied were:

- **Magnetic Fields:** The magnetic environment is crucial in NMOR, thus shielding and magnetic field control must be understood and calibrated. Maps of the magnetic fields inside the shield are useful in determining the quality of our magnetic environment. Other magnetic parameters studied include degaussing of the shield and the sweep rate of the magnetic fields.
- **Laser parameters:** Tuning the laser to near resonance peaks is important to achieve maximum optical rotation. Also, the intensity of the beam is critical to maximizing the signal. This was studied further to determine the optimal laser power.
- **Cell quality:** Initially, the quality of the cell was not expected to be a major systematic error. Nevertheless, the low quality of the cell became apparent after other modifications to the system were not as effective as expected. We modified the cell using heat and built an apparatus to quantitatively measure cell parameters which we could then compare to known higher quality cells.

Furthermore, bandwidth limitations of our AM NMOR system used for nonzero field NMOR were also examined experimentally. The newly optimized system was then tested as a functioning all-optical magnetometer.

# Chapter 2

## Theory

### 2.1 Linear Faraday Rotation

When linearly polarized light passes through a medium subjected to an axial magnetic field, the plane of polarization emerges rotated. The rotation is known as the Faraday effect. Ultimately, this effect can be related to Zeeman shifts in atomic levels in the medium. This is sometimes called the Macaluso-Corbino effect [8]. To illustrate this effect, consider the example  $F = 1$  to  $F' = 0$  transition (Fig. 2.1) where  $F$  is the relevant total angular momentum quantum number. Linearly polarized light may be considered as a superposition of two counter-rotating circularly polarized components with respective resonance frequencies  $\sigma^\pm$  with respective  $\Delta M = \pm 1$  selection rules where  $M$  is the magnetic quantum number related to  $F$ . In the presence of a magnetic field, the Zeeman sublevels  $M = \mp 1$  shift in energy by an amount  $\mp g\mu B/\hbar$  where  $g$  is the Lande factor and  $\mu$  is the Bohr magneton. Consequently, the resonance frequencies for  $\sigma^\pm$  light also shift in energy. Each circular polarization experiences a different index of refraction  $n_\pm$ . The difference in  $n_\pm$  gives rise to an optical rotation

$$\phi = \pi(n_+ - n_-)\frac{l}{\lambda} \quad (2.1)$$

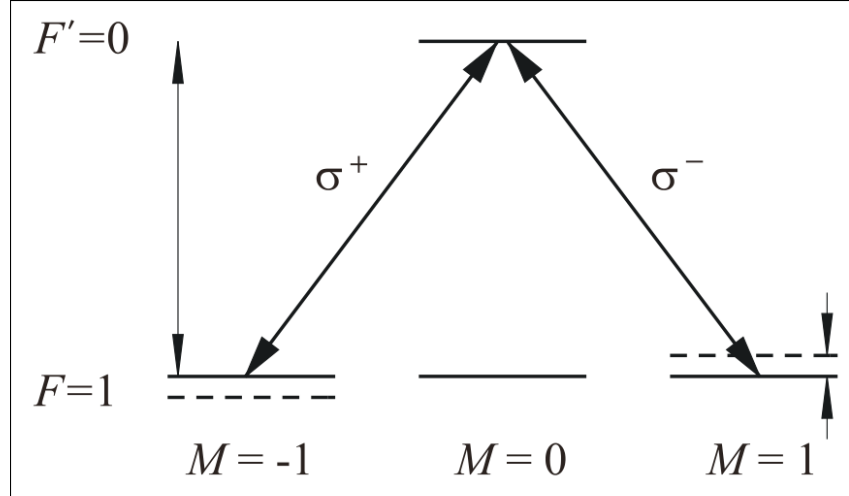


Figure 2.1: Illustrative example of  $F = 1$  to  $F' = 0$  atomic transition with Zeeman splitting in the presence of a magnetic field taken from [8]. Vertical axis = energy. Horizontal axis =  $M$ .  $\sigma^+ \rightarrow \Delta M = 1$  and  $\sigma^- \rightarrow \Delta M = -1$ . The resonance energies are shifted for each circularly polarized state.

where  $l$  is the length of the medium traversed and  $\lambda$  is the wavelength of light. On resonance, the rotation is related to the Zeeman shift in the  $M = \mp 1$  sub levels. The optical rotation can be estimated as

$$\phi \approx \frac{2g\mu B/\hbar\Gamma}{1 + (2g\mu B/\hbar\Gamma)^2} \cdot \frac{l}{l_0} \quad (2.2)$$

where  $2g\mu/\hbar$  is correlated to Zeeman splitting,  $\Gamma$  is the doppler width of the absorption line (of order GHz), and  $l_0$  is the absorption length in the medium [8]. Linear optical rotation has widths  $\sim 400$  G (Gauss) where width is defined as the separation between the peak and valley as explained in Sect. 1.2.

## 2.2 NMOR

Achieving ultra-narrow optical rotation widths relies on nonlinear effects. In our context, nonlinear refers to the medium's susceptibility to light and the ability of the light to change the properties of the medium. This is done simultaneously by two methods: hole burning and coherence effects.

When light enters the medium, atoms absorb energy which increases their atomic velocity. This depletes the ground state atomic velocity distribution at a certain velocity and creates a 'hole'. Since the hole is much narrower ( $\sim$ MHz) compared to  $\Gamma$  ( $\sim$ GHz), the resulting rotation is increased and feature widths are correspondingly decreased.

Further narrowing of the feature width arises due to coherence effects in the ground state Zeeman sub levels. Again considering the  $F = 1$  to  $F' = 0$  transition example (Fig. 2.1), the medium can be thought to be in a superposition of ground states given by

$$\frac{1}{\sqrt{2}}(|M = 1\rangle + |M = -1\rangle) \quad (2.3)$$

$$|M = 0\rangle \quad (2.4)$$

$$\frac{1}{\sqrt{2}}(|M = 1\rangle - |M = -1\rangle) \quad (2.5)$$

If incident linearly polarized  $\chi = \sigma^+ + \sigma^-$  light enters the medium, it depletes the state  $\frac{1}{\sqrt{2}}(|M = 1\rangle + |M = -1\rangle)$  corresponding to the plane of polarization. The medium eventually becomes transparent to light  $\chi$ , yet light of orthogonal polarizations would still be absorbed. The remaining coherent superposition of  $|M = 0\rangle$  and  $\frac{1}{\sqrt{2}}(|M = 1\rangle - |M = -1\rangle)$  is known as a dark coherent superposition, referred to as a dark state. As the atoms are pumped into this dark state, the medium becomes linearly dichroic (absorption of light is dependent on polarization), much like a linear polarizer. The axis is called the axis of alignment.

At the atomic level, the magnetic moments of the atoms are oriented with respect to the axis of alignment. In a magnetic field, the aligned moments experience a torque and precess around the axis of the field at the Larmor frequency (much like a set of linear polarizers). The net result is a medium that is circularly birefringent (index of refraction is dependent on the circular polarization state). Optical rotation is now a measure of the angle of rotation of the dichroic medium (polarizers) in relation to orthogonal polarizations.

As it turns out, the angle of rotation can again be estimated by Eq. 2.2 with  $\Gamma \rightarrow \gamma_{rel}$

$$\phi \approx \frac{2g\mu B/\hbar\gamma_{rel}}{1 + (2g\mu B/\hbar\gamma_{rel})^2} \cdot \frac{l}{l_0} \quad (2.6)$$

where rotation is now limited only by to the relaxation rate  $\gamma_{rel}$  of atomic alignment. Large rotation with narrow widths result from longer atomic relaxation times. Studies into  $\gamma_{rel}$  are discussed in detail in Ch. 4.1.4

Optical rotation widths thereby decrease in size from hundreds of Gauss to  $\sim \mu\text{Gauss}$ . Figuratively, a comparison between linear and nonlinear effects is shown in Fig. 2.2. Narrower widths allow for a more sensitive magnetometer.

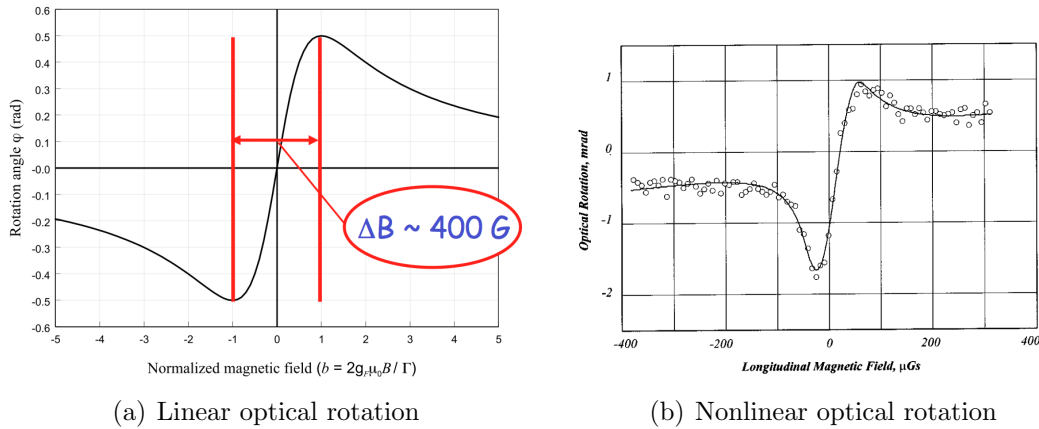


Figure 2.2: Comparison showing the drastic narrowing of the optical rotation feature between linear and nonlinear effects. The narrowing is due to a combination of hole burning and a coherent dark superposition of states. Figures taken from [9] and [8] respectively.

The narrowest widths published to date are  $2.8 \mu\text{G}$  separation [6]. This was achieved on the  $D_2, S_{1/2} \rightarrow P_{3/2}$  resonance line of  $^{85}\text{Rb}$  using a paraffin coated vapour cell. See Ref.[10] for further discussion of the hyperfine structure of Rb.

## 2.3 AM NMOR

In order for NMOR to be observed at non-zero fields, the laser light must be either AM or FM. Modulated NMOR in this thesis focused on AM NMOR us-

ing an acousto-optic modulator (AOM). Recalling the rotating polarizer analogy, if the polarizer rotates at the Larmor frequency, modulating the light at twice the Larmor frequency will essentially negate the effects of rotation, resulting in a stroboscopic effect. This is because the light is flashing on at exactly the same alignment relative to the rotating atomic structure of the medium. Modulating pump light at this specific frequency creates a resonance which can then be measured using a subsequent probe beam. Measuring NMOR on this resonance allows for narrow widths to be observed in non-zero fields, and thus non-zero field magnetometry. In Ref.[1], a remote all-optical magnetometer was demonstrated with a sensitivity of  $\sim 3$  nG in Earth's field. In order to accomplish this in Earth's field, they were able to modulate an AOM at upwards of a MHz. This again was achieved using a paraffin coated Rb cell, tuned to the  $D_2$  line in  $^{87}\text{Rb}$ .

Potential limitations on this AM NMOR system are due to the AOM and the photodiode. Essentially, the rate in which the light is able to be modulated and how well the photodiode can detect modulations in light. These potential limitations are addressed quantitatively in Ch. 4.2.

## 2.4 Relaxation Time

Since optical rotation is a function of the atomic relaxation time of the cell, a system to measure the relaxation rate  $\gamma_{rel}$  is useful to quantify cell quality. After the incident laser light creates the aligned state, the time scale  $\tau_{rel} = 1/\gamma_{rel}$  is the time in which the atoms relax to an unaligned state. The time scale is dependent on cell quality because generally wall collisions destroy the alignment. It has been found explicitly that paraffin coating reduced the likelihood of relaxation.  $\gamma_{rel}$  must then be driven by the likelihood of atoms to return to the solid Rb reservoir.

To measure the relaxation time, a pump beam of circularly polarized light is used to align the atoms along the magnetic field by optical pumping. The pump beam is then blocked allowing the atoms to relax over time. Optical rotation of

the probe beam is used to measure the relaxation time via optical pumping done in a relatively large axial magnetic field  $\sim 15$  G. Blocking the pump beam while continuously measuring the probe beam shows an exponential decay of optical rotation characterized by

$$\phi \approx e^{-\frac{t}{\tau_{rel}}} = e^{-\gamma_{rel}t} \quad (2.7)$$

hence giving a direct measurement of  $\gamma_{rel}$  and the quality of the cell.

Prolonging the atomic alignment is crucial to achieving ultra-narrow NMOR resonance widths. The best cells with the longest relaxation time are made by M. Balabas [11]. A relaxation time measurement is shown in Fig. 2.3. Further

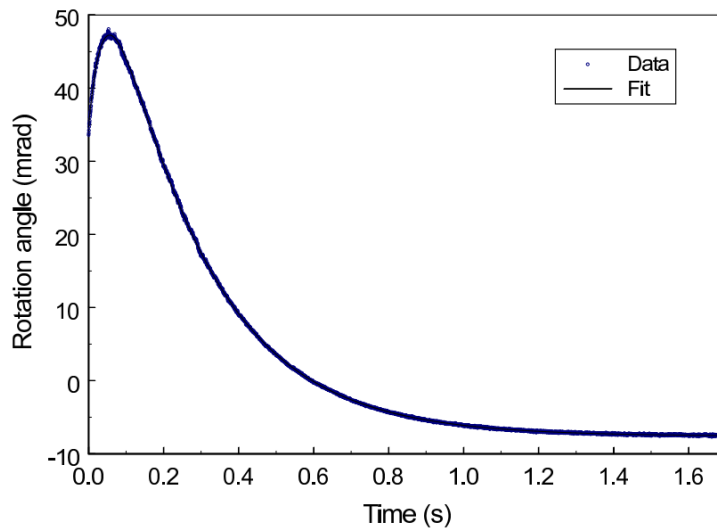


Figure 2.3: Relaxation time measurement taken from Ref.[7]. Data was taken using a high quality cell made by Balabas.  $\tau_{rel} = 1/\gamma_{rel}$  measured to be of order seconds.

discussion into the theory and characterization of these cells can be found in Ref.[7].

# Chapter 3

## Experimental Set Up

### 3.1 Laser

Experiments were conducted at the University of Winnipeg in room 3L11. A Toptica DL-100 tunable diode laser was used and positioned on an optics bench. The laser outputs a tuneable wavelength near 795 nm with an output power  $<100$  mW. The laser spot size is elliptical, and approximately  $3 \text{ mm} \times 5 \text{ mm} = 15 \text{ mm}^2$ . The laser was typically tuned to the  $D_1 \text{ F} = 3,2 \rightarrow 2$  absorption minimum and then adjusted to maximize optical rotation. Our NMOR system uses an atomic vapour cell containing natural rubidium with stable isotopes  $^{87}\text{Rb}$  and  $^{85}\text{Rb}$  both being present.

### 3.2 NMOR

A diagram of the apparatus used for NMOR measurements near zero field is shown in Fig. 3.1. The laser beam is split using a beamsplitter (thin glass slide glued to an optical mount). The beam then passes through an interchangeable neutral density filter used to control light intensity. The initial beam output is polarized, but a second polarizer is used to ensure a pure linearly polarized beam. A half wave plate is then used rotate the axis of polarization near 45 degrees. The

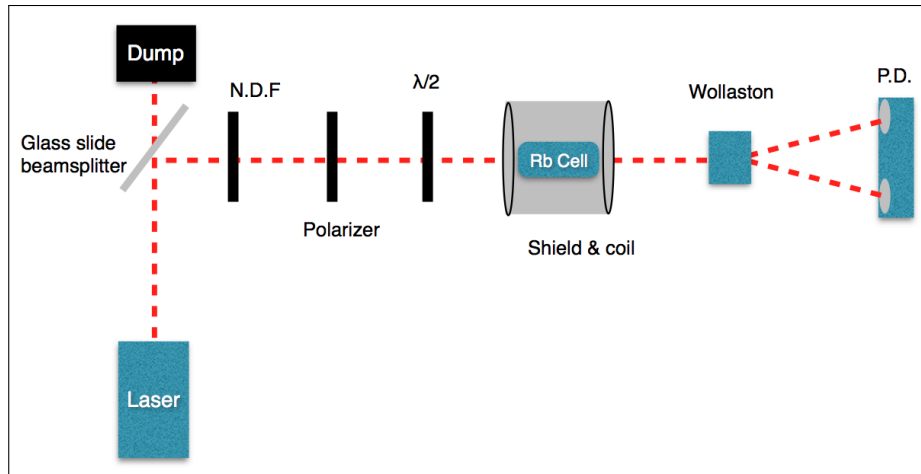


Figure 3.1: NMOR experimental set up. N.D.F - neutral density filters used to control light intensity. P.D. - New Focus dual photodiode purchased warranted by results discussed in Sect. 4.2.

majority of the beam passes through the beamsplitter and into the light dump, and generally the remaining beam operates at low power  $\sim 30 \mu\text{W}$ . The beam then passes through our vapour cell which sits inside a magnetic shield. Inside the shield is a coil designed to apply well controlled fields both on and off the axis of light. The coil is supplied with a voltage from a variable power supply which can also sweep the magnetic field about zero. A Wollaston is used to split the beam into its perpendicular polarization axes which are then analyzed individually by our photodiode. Our photodiode contains two individual diodes and an internal differential amplifier which outputs the difference in diodes  $P_1 - P_2$ . Note that in the absence of a cell and the half wave plate orienting the linear polarizer at 45 degrees, the differential photodiode should register zero. Using Malus' Law, it can be shown that for small  $\phi$ ,

$$\phi = \frac{P_1 - P_2}{2 \cdot (P_1 + P_2)} \quad (3.1)$$

in radians where  $P_{1,2}$  are the photodiode outputs in volts. It must be noted that due to our photodiode outputting the difference  $P_1 - P_2$ , it was often difficult to measure  $P_1$  and  $P_2$  individually. This was done periodically to measure  $\phi$  in

radians, but it was not always done. Since the optical rotation is small ( $\sim 1$  mrad),  $P_1 + P_2$  is essentially constant. Often, we will therefore display optical rotation in units of volts or in arbitrary units.

### 3.3 AM NMOR

A similar set up using a pump-probe technique was used to study AM NMOR. This is shown in Fig. 3.2. The incident beam passes through two beamsplitters used to split the beam into the pump and probe beams. Similar to Sect. 3.2, the pump/probe beams are both  $\sim 30 \mu\text{W}$  in power. Beam 1 (probe) follows the same path as Sect. 3.1. Beam 2 (pump) is focused by lens 1 to a dot size of  $< 2$  mm in order to pass through the AOM crystal. A second lens after the AOM is needed to stop the beam from diverging to infinity. Once through the crystal, the pump beam now flashes at a frequency controlled by an electrical signal applied to the AOM. Mirrors then aim the pump beam into the cell nearly coaxially with the probe beam. Due to optical components on the table in the beam line, there was a small angle between the pump/probe beams. The pump beam nearly crosses the probe beam at the centre of the cell. After passing through the cell, the pump beam is blocked in a beam dump. The probe beam is again split into polarization axes and detected individually with a single output of  $P_1 - P_2$ .

### 3.4 Magnetic Shielding

Our previous set up consisted of a single layer, uncapped magnetic shield. Inside the shield, a coil was wound around a cardboard tube and held in place with bubble wrap. This set up made it difficult to control magnetic fields and optical alignment. A new four layer magnetic shield was received midway through completion of this work and a new coil was wound and characterized. Fig. 3.3 shows a comparison of the old and new shield.

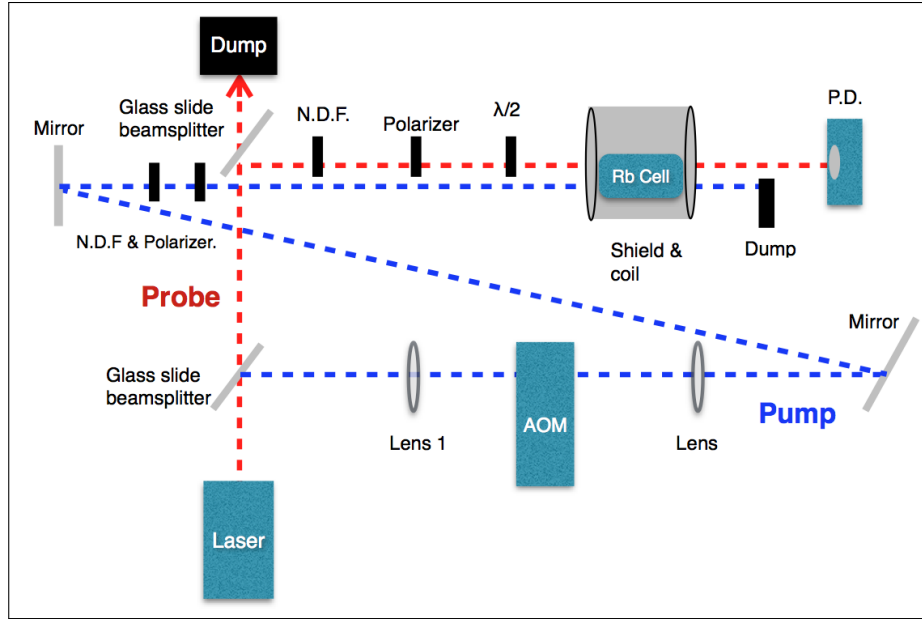


Figure 3.2: AM NMOR experimental set up. N.D.F - neutral density filters used to control light intensity. P.D. - Various photodiodes as discussed in Sect. 4.2. AOM - Acousto-optic modulator

The new shield was designed with a region of interest (ROI) of four inches at the centre of the shield. Homogeneity in the ROI is important as the vapour cells encompass this region. Using a fluxgate magnetometer, the interior of the shield (with the end caps on) was magnetically mapped. The fluxgate was inserted from both the east and west ends of the shield and measured at one inch increments over the length of the shield. Degaussing of the inner most shield was also studied (further discussion in Sect. 4.1.2). Fig. 3.4 shows a comparison of before and after degaussing. We observed homogeneity in the ROI and degaussing only important at low residual fields. Before degaussing, residual magnetic fields of order  $10 \mu\text{G}$  were present. After degaussing, residual fields were decreased to  $<5 \mu\text{G}$ . At this stage in our NMOR system, NMOR widths of order  $>100 \mu\text{G}$  have been achieved. Thus, the new shield and degaussing of the shield has improved the magnetic environment to a level sufficient for our present set up. Once NMOR widths are achieved to the same order as the residual fields in the ROI, further improvements in magnetic shielding will need to be addressed. This will likely be done using the

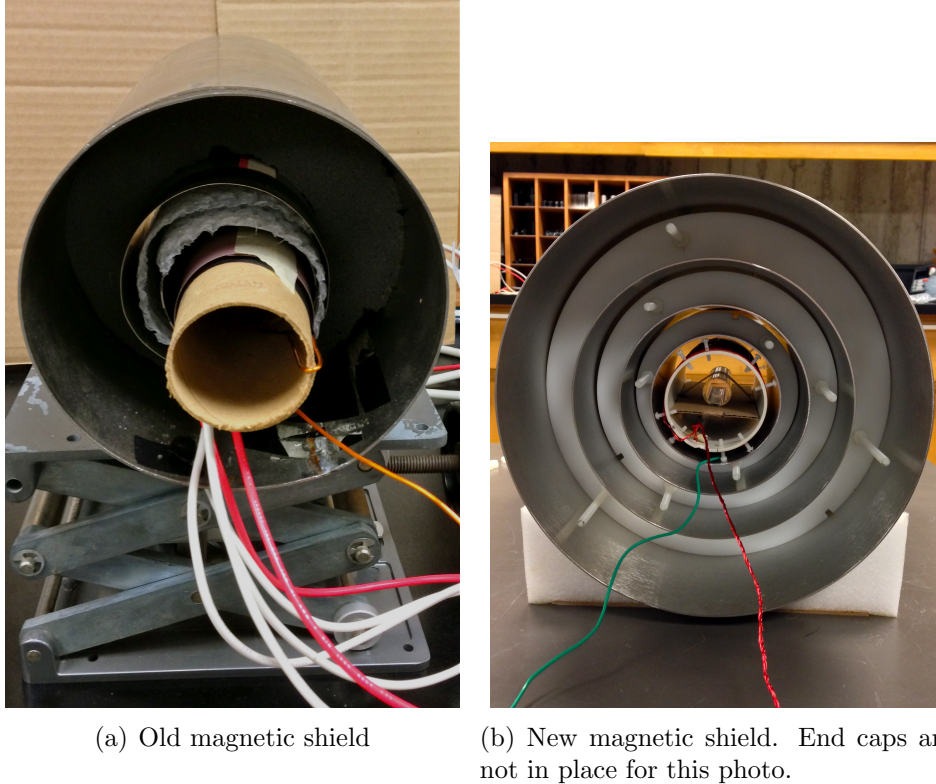


Figure 3.3: Old and new magnetic shielding for our NMOR set up. The respective coils are inside, along with a loop of degaussing wire.

NMOR system itself as a probe because the fluxgate magnetometer used for the mapping appears to be nearing the limit of its sensitivity.

### 3.5 Internal Coil

A new coil was wound on a plastic tube to fit inside the new magnetic shield (see Fig. 3.5). It was designed to create a uniform magnetic field axially in the direction of light propagation ( $\hat{z}$ ) as well as fields in the off axis ( $\hat{x}$  and  $\hat{y}$ ) directions. The off axis coils were wound around screws 120 degrees apart with main windings running along the axial  $\hat{z}$  direction.

To generate a current through the coil, a power supply operating in voltage mode was attached in series with a variable resistor normally set at 1 k $\Omega$ . The circuit is shown in Fig. 3.6.

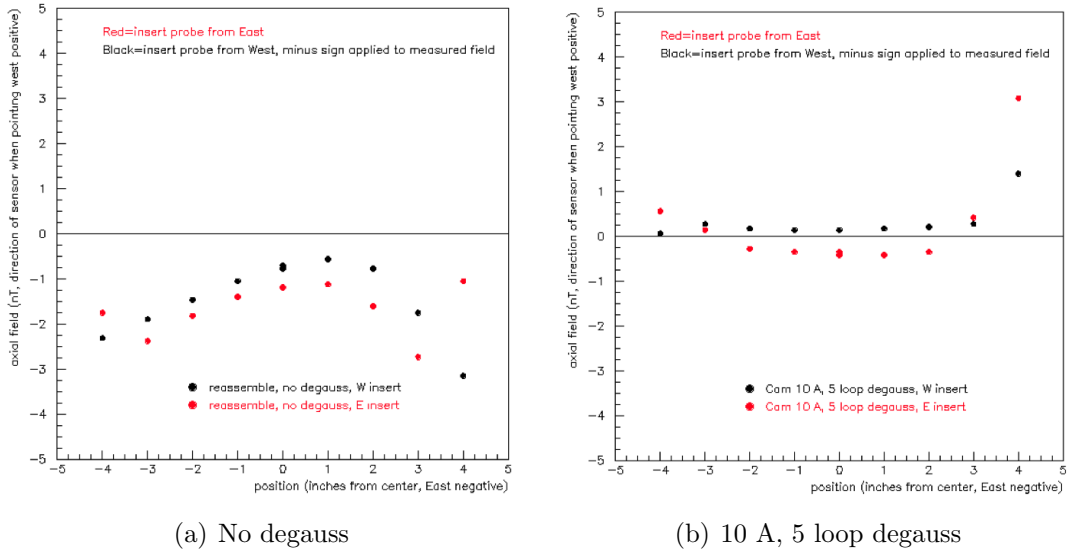


Figure 3.4: Magnetic field maps for the new magnetic shield before and after degaussing. Maps done with a fluxgate magnetometer inserted from the east and the west with respect to the shield. Homogeneity is needed through the four inch cell length at the center. For reference,  $1 \text{ nT} = 10 \mu\text{G}$ .

We used a fluxgate magnetometer to calibrate both the old and the new coils.. The output from the fluxgate was then graphed with respect to the voltage supplied by the power supply as it modulated the field. A linear fit then resulted in a calibration in units of  $\mu\text{G}/\text{V}$ . For the old coil/shield our calibration constant was  $B = 8600 \mu\text{G}/\text{V}$  while the new coil/shield yielded a value of  $B = 480 \mu\text{G}/\text{V}$ . The linear fits are shown in Fig. 3.7.

Calibration of the off-axis coils and impacts on the NMOR system will be discussed further in Ch. 4.1.2.

## 3.6 Relaxation Time

The optical bench set up to measure the relaxation time of paraffin coated cells is shown in Fig. 3.8. The incident beam is again split into two beams using a beamsplitter. The pump beam goes through a mechanical shutter to act as a temporary beam blocker. The pump beam typically operated at a high power  $\sim 3$



Figure 3.5: Coil for the new magnetic shield. Off axis field coils wound parallel to the centre axis of the tube.

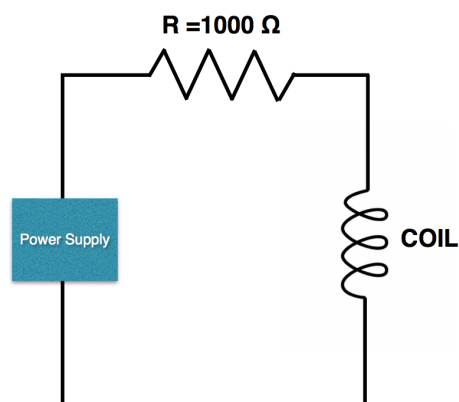


Figure 3.6: Power supply in series with a variable resistor and the coil. The power supply used most frequently was a Wavetek 130, though an Agilent 33210A waveform generator was used for more accurate field control.

mW to ensure alignment along the axis, while the probe beam was much lower power ( $\sim 30 \mu\text{W}$ ). The mechanics of the shutter was found to be too slow for the short relaxation times measured. It also caused vibrations on the table which resulted in noise in the system. So often a simple hand wave was used in place of the shutter to act as a faster beam blocker for final data acquisition. After the shutter, the pump beam passes through a linear polarizer and quarter wave plate which converts the linearly polarized light into circularly polarized light. Mirrors then direct the pump beam towards the cell. The pump and probe beams cross

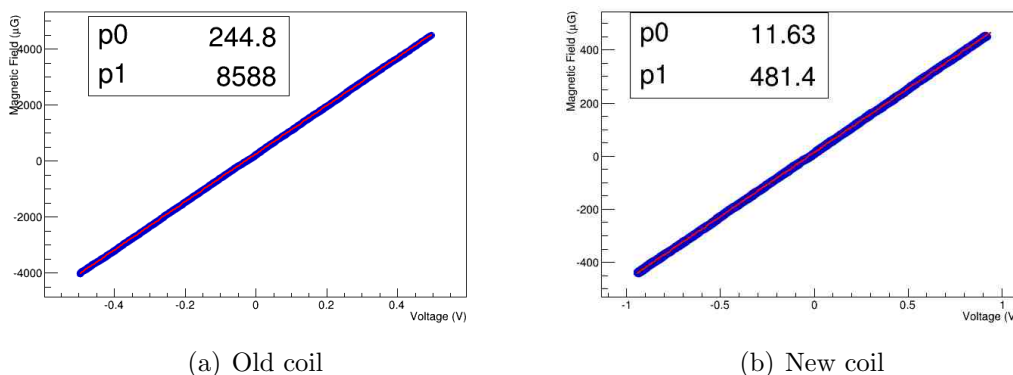


Figure 3.7: Magnetic field as measured by a fluxgate versus supplied voltage. Linear fit to determine the calibration coil constants for both the old and the new coils in  $\mu\text{G}/\text{V}$ .

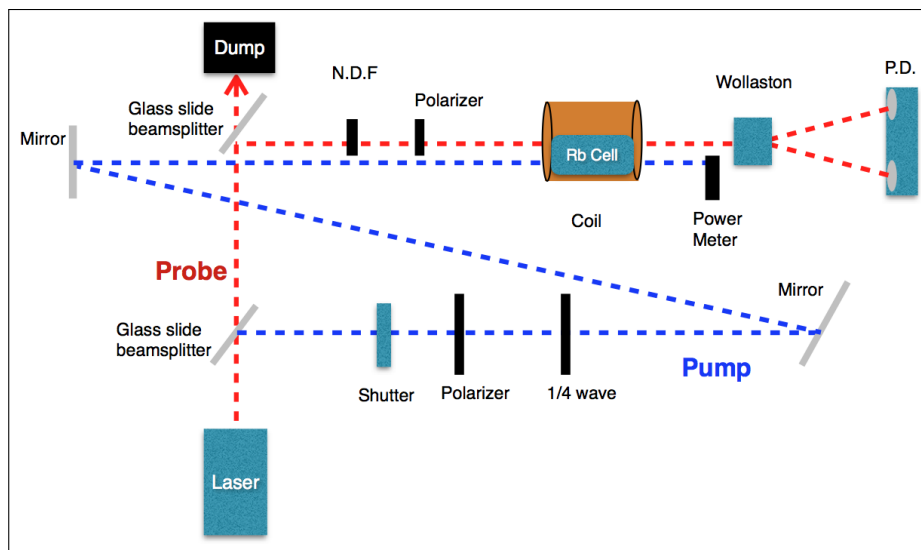


Figure 3.8: Relaxation time experimental set up. N.D.F - neutral density filters used to control light intensity. P.D. - New Focus dual photodiode. Larger coil is capable of applying large axial fields and eliminates the need for shielding.

at the centre of the cell inside the coil. This experiment is performed at large magnetic fields (larger than Earth's field) so shielding is unnecessary. The coil used is capable of supplying  $\sim 15$  G fields. Optical rotation is measured by the probe beam using a Wollaston and detected by the photodiode. A Newport power meter measures the pump beam.

# Chapter 4

## Data Analysis

### 4.1 NMOR near Zero Field

Improvements to the system were designed to narrow the NMOR width attempting to get as close as possible to the  $\sim \mu\text{G}$  level demonstrated previously in Ref. [6] and Fig. 1.1. In the end, we were able to narrow the width by a factor of ten by studying and improving upon various parameters. Furthermore, we developed a tremendously better understanding of what limits the system presently. The progression of our results throughout the year is shown in Fig. 4.1. Initial resonance widths were in the thousands of  $\mu\text{G}$ . We were able to narrow the NMOR feature substantially, reducing the width to  $\sim 150 \mu\text{G}$  over the course of this work. This is approaching the work done by [8], but improvement must still be done to reach the narrowest published width of  $2.8 \mu\text{G}$  [6]. Systematically, each important system parameter was studied, including magnetic parameters, laser parameters, and cell quality. We then tested the optimized system as a magnetometer at zero field to demonstrate the present magnetometric sensitivity. In the end, it was discovered that cell quality was the chief factor limiting further progress.

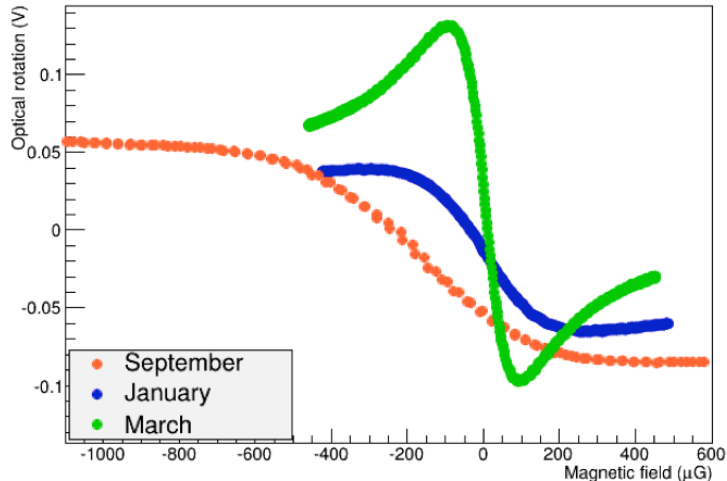


Figure 4.1: An overlay of NMOR progression as taken through September 2013 and March 2014. Laser tuned near  $^{85}\text{Rb}$   $F = 3-2,3$  absorption minimum. NMOR widths reduced from  $\gtrsim 1000\mu\text{G}$  to  $\sim 150\mu\text{G}$ .

### 4.1.1 Fit Analysis

As stated previous, optical rotation is approximated by Eq. 2.6. We are able to fit our data to this functional form, such that

$$\phi = \frac{aB}{1 + (aB)^2} \cdot l + C \quad (4.1)$$

where  $l$  and  $C$  are in units of volts, and  $a$  in units of  $1/\mu\text{G}$ . Minimizing Eq. 4.1, the peak and valley of the NMOR feature can be found to be

$$P, V = \frac{1}{a} \quad (4.2)$$

Since the NMOR feature is symmetric about zero field, the total width of the feature is  $2 \times 1/a$  in  $\mu\text{G}$ . Thus,  $a$  is the significant parameter of our fit.

### 4.1.2 Magnetic Parameters

#### Shielding

As discussed previous in Sect. 3.4, a new magnetic shield was received designed specifically for our set up. When placed in our pre-existing NMOR set up, it

was a clear improvement over the latter shield. In Fig. 4.1, September (orange) to January (blue) shows the progression of simply changing the magnetic field shielding and generation. Since we have residual magnetic fields present in the 1-10  $\mu\text{G}$  level, NMOR widths of 500  $\mu\text{G}$  are unaffected. Once our NMOR widths decrease to this residual level, magnetic shielding must be addressed once more.

### Degaussing

Our magnetic shield is designed to minimize the magnetic field at the cell, but magnetic hysteresis limits the magnetic field in any region to be exactly zero. Remnant magnetic field is able to be decreased or eliminated by a process called degaussing. This involves inducing a magnetic field at the shield by passing current through a wire.

The design of the magnetic shield end caps do not leave sufficient room to feed through multiple degaussing coils and still pass a laser beam through. Optimal degaussing involves individual loops of wire wound tight about each shield layer separately, however, this will take further design to fit the wires inside the shield. All degaussing was done with a single wire through the inner most shield. Any residual fields due to outer layers will be assumed shielded by the inner most layer, thus degaussing is most beneficial at the inner most layer and looping out around the outermost shield.

Similar to magnetic shielding, degaussing was concluded as a non-factor at this width. This was confirmed by comparing the width pre and post degauss. As shown in Fig. 4.2, the discrepancies are small relative to the overall width. It must be noted that the decrease in width was due to data taken at a later date with a post heat gunned cell and not the degaussing. Details of heat gunning the cell are discussed in Sect. 4.1.4. Respective fits yielded parameters  $a_{before} = 0.01075$   $1/\mu\text{G}$  and  $a_{after} = 0.01068$   $1/\mu\text{G}$  which correspond to NMOR widths of 186  $\mu\text{G}$  and 187  $\mu\text{G}$ . This is consistent with Sect. 3.4 as effects of degaussing the shield are

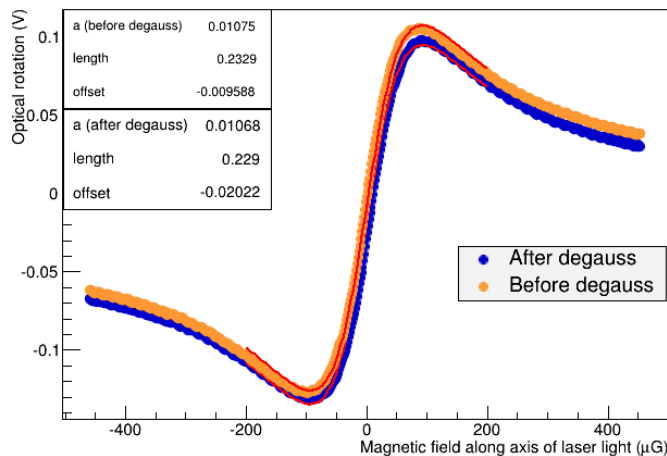


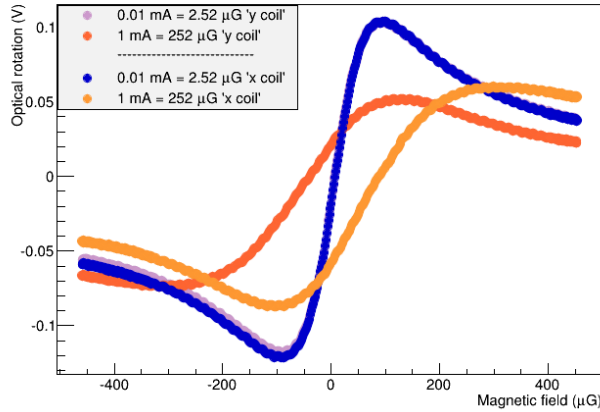
Figure 4.2: NMOR widths taken before and after a 10 A degauss of the inner most shield. The cell used was post heat gun. The data was fit to Eq. 4.1.

of order  $\lesssim 10 \mu\text{G}$ . Once resonance widths are achieved to this threshold, designing a multiple wire degaussing system that fits in the shield may be of interest.

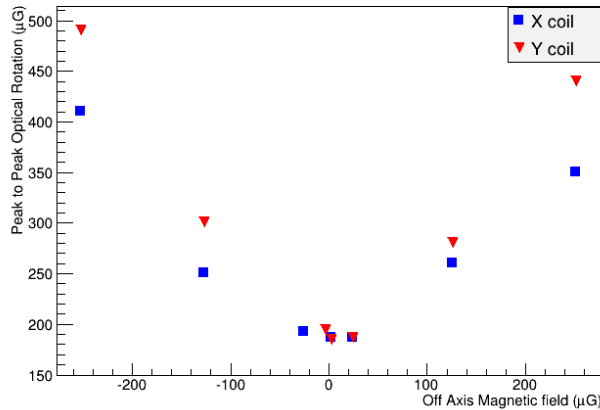
### Off-Axis Fields

Another important aspect of magnetic shielding is to be able to understand and control the off-axis fields. In Ref. [6], they were able to broaden the NMOR width using transverse magnetic fields greater than the NMOR width. Thus similar to the discussion of magnetic shielding and degaussing, off axis fields must be controlled well once the resonance width is of the same order of magnitude. The coil built was calibrated inside the magnetic shielding. We used a fluxgate magnetometer to measure the fields in the  $\hat{x}$  and  $\hat{y}$  direction respectively. This fluxgate was too large to fit through the end caps of the shield, so calibration had to be performed without end caps. This gave calibration constants of  $B = 0.0252 \mu\text{T}/\text{mA}$  for both directions. It must be noted that it is unclear as to which direction is x and y relative to the direction of light polarization. While the coils were orthogonal to one another, they were oriented at 45 degrees relative to the

light polarization direction, contrary to the convention used in Ref. [6, 8] where  $\hat{x}$  is oriented along the polarization direction. It is also unclear which x and y were oriented vertically and horizontally, although this distinction is likely irrelevant.



(a) Broadening of NMOR widths



(b) NMOR widths versus field strength

Figure 4.3: Dependence of NMOR width on off-axis field strengths. (b) shows the threshold in which off-axis fields begin to broaden the width.

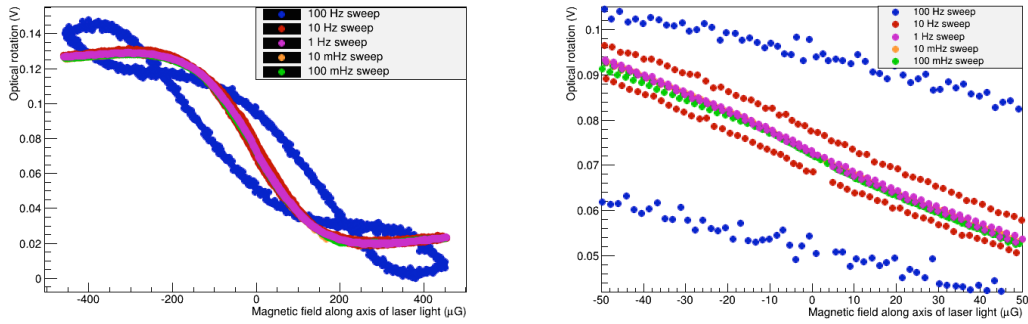
Setting the system at maximum rotation, we then varied the current to the off-axis coils. At low fields ( $\sim 3 \mu\text{G}$ ), the widths were unaffected, but as we increased the off axis fields ( $\sim 250 \mu\text{G}$ ), the resonance widths broadened substantially. The broadening became substantial only as the fields exceeded the NMOR width, consistent with the results found from magnetic shielding and degaussing. It is

also consistent with the expectation based on Ref. [6, 8]. Fig. 4.3(a) shows of broadening of the widths and Fig. 4.3(b) summarizes the progression of peak to peak NMOR widths at different off axis field strengths.

We were able to essentially saturate any rotation signal measured with off-axis magnetic fields. Thus with the new coil, we are now able to control the off-axis fields to 1/100th of the present NMOR width at the  $\mu\text{G}$  level. This follows the same trend as the magnetic properties and is optimized to a level above the state of our system. Once NMOR widths narrow, improved control of off axis fields should be reinvestigated with care taken in the orientation of the coils.

### **Magnetic Sweep Rate**

In these studied, the magnetic field was usually swept using a waveform generator outputting at triangle wave. It was noticed that, depending on the sweep rate, the optical rotation signal displayed two features dependent on the sweep direction, whether increasing or decreasing. These two different features are dependent on the frequency of the triangle wave. It was discovered that at slow sweep rates ( $<100$  mHz), the dependence of sweep direction was small, but at faster rates (Hz) the symmetry diminishes and the features broaden. However, sweeping slowly requires minutes of data acquisition and is not practical to make any fine adjustments to the system as needed. Fig. 4.4 shows the difference in faster versus slower sweep rates. From Fig. 4.4(b) it is clear that for sweep rates slower then 1 Hz the margin of difference is small and there is a high degree of symmetry between the up-sweep and down sweep. Most of our data was taken at 1 Hz since the differences are marginal at low frequency. This conclusion agrees with Ref.[12] where ripples in the optical rotation signal are seen at high sweep rates after passing through zero field.



(a) NMOR feature for various sweep rates (b) Zoom of Fig. 4.4(a) in the centre region about zero

Figure 4.4: Optical rotation versus magnetic field for various sweep rates. Zooming in around zero field shows little discrepancy at slow sweep rates.

### 4.1.3 Laser Parameters

#### Power

Optical rotation also depends on the light intensity of the beam. As previously stated, the laser outputs a dot size of approximately  $0.15 \text{ cm}^2$ . Previous work (Ref.[6, 8]) operated at low beam intensities of  $\sim 100 \mu\text{W}/\text{cm}^2$ . It is possible to supply a larger current to the laser diode to output more power; however, this alters the tune of the laser and requires changing the diode temperature. So, once the laser was tuned to the resonance minimum, interchangeable neutral density filters were used to adjust the intensity of the beam at the cell. They range in opaqueness and allow different amount of light to pass. Using the NMOR apparatus (Fig. 3.1) an optimized rotation signal was acquired, then a power meter was placed directly in the incident beam path just before the cell to measure the laser power. The peak to peak widths were then graphed versus laser power (Fig. 4.5). Due to the limited number of neutral density filters, only select beam intensities were available. The beam powers thereby achieved were 20, 38, 77, and  $463 \mu\text{W}$  with additional background light of  $4 \mu\text{W}$ . Noticeable degradation of the signal appeared at low light intensities as there was not enough light to sense in the photodiode. At high power the resonance widths broadened substantially

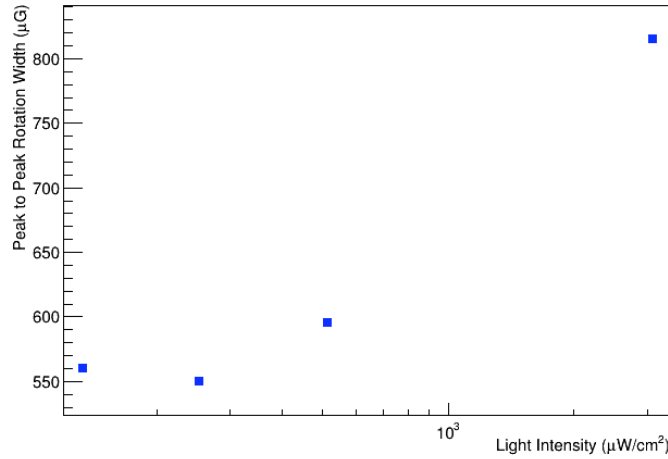


Figure 4.5: NMOR widths versus light intensity at the cell. Light intensity is shown on a log scale using a dot size of  $0.15 \text{ cm}^2$ .

due to over saturation of the sample causing the sample to become transparent. As shown in Fig. 4.5, there is a range of useable powers from  $30 - 70 \mu\text{W}$  where the effects on narrowness is negligible. Thus, the optimal power for our set up is approximately  $38 \mu\text{W}$ . This was achieved using the single density filter labeled /28, and this was the normal set up used in the probe beam for all experiments. This corresponds to a light intensity of  $230 \mu\text{W}/\text{cm}^2$  which is above the  $100 \mu\text{W}/\text{cm}^2$  used in Ref.[6], though still within our threshold due to power broadening.

### Frequency Detuning

When tuning the laser, there must be a slight detuning from the absorption minimum to achieve maximum optical rotation signal. This also does not happen at exactly zero field. It is important to control and measure the frequency detuning required to maximize the relative to the Rb absorption minimum. In an ideal system, a feedback system would be used to set the tuning or "lock" the laser (see Sect. 5.2).

Fig. 4.6 compares optical rotation signals at various static magnetic field

strengths with respect to the relative frequency of the absorption spectrum of our natural Rb vapour cell. The horizontal axis has been calibrated to the absorption spectrum in the lowest panel.

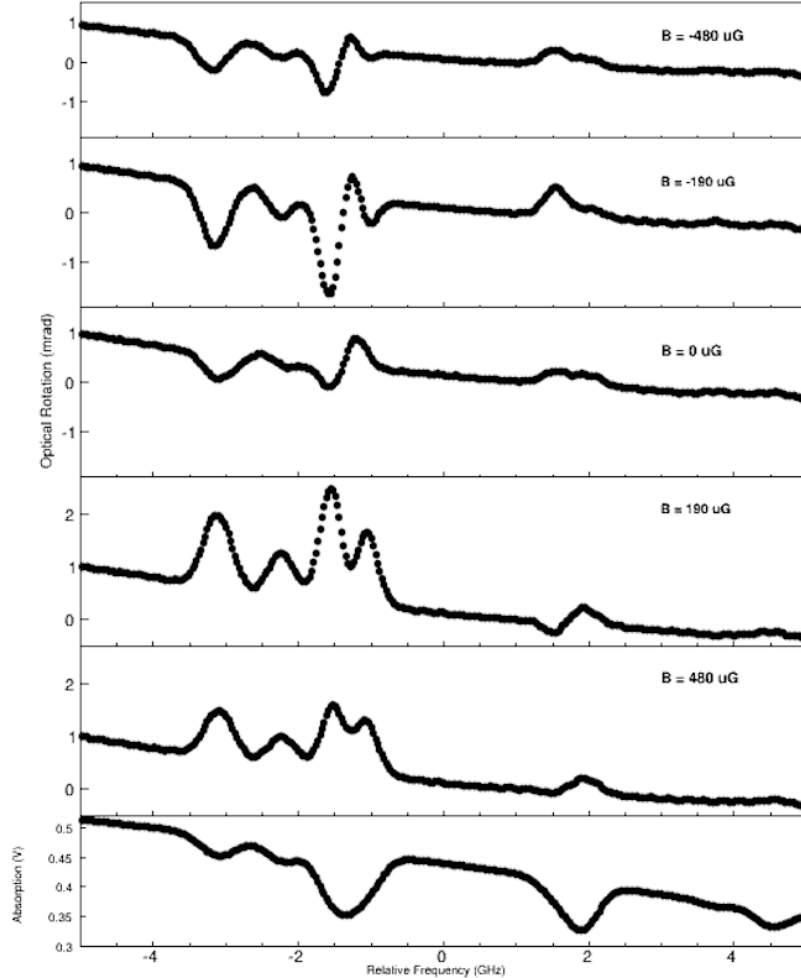


Figure 4.6: Optical rotation versus relative frequency of the  $D_1$  Rb line. The bottom trace shows the absorption spectrum of our vapour cell containing both  $^{85}\text{Rb}$  and  $^{87}\text{Rb}$  isotopes. For various static magnetic field strengths, optical rotation is maximized and slightly detuned to the minimum. Frequencies calibrated with respect to the  $^{85}\text{Rb}$  fine structure and frequencies taken from Ref.[10].

An arbitrary zero point was set with respect to the fine structure of  $^{85}\text{Rb}$  [10]. All other frequencies were calibrated from this by assigned relative frequencies to the voltage of each peak. The resonance we most frequently tuned to was the  $F=3,2 \rightarrow 3$  transition of  $^{85}\text{Rb}$  situated at  $\sim -1.4$  GHz in Fig. 4.6. Corresponding

maximum optical rotation occurred with a slight detune of  $\sim -0.3$  GHz from the absorption resonance at a magnetic field strength of  $\pm 190 \mu\text{G}$ .

#### 4.1.4 Cell Quality

##### Cell Improvements

Once magnetic fields were improved and laser parameters were studied, the only remaining course was to examine cell parameters. The vapour cell was a 4 in. long, 1 in. diameter glass cylinder with a small stem. Inside, natural rubidium containing both isotopes 85 and 87 would ideally be kept in the stem, used as a reservoir, and the walls of the cylinder coated in paraffin wax in order to prolong atomic alignment after wall collisions. Thus, atoms in the coherent dark state would be less likely to collide with unpolarized atoms absorbed on the wall. This would lengthen the time atoms spend in the coherent dark state. Ref. [7] discusses the theory behind the best paraffin coated vapour cells and their characterization.

Our cell was purchased from Precision Glassblowing and possessed only some of the qualities of the best cells. Initially, our cell appeared cloudy with no prominent reservoir in the stem. The rubidium was visibly smeared over the cylinder wall opposite the stem. When the atoms are aligned, collisions with unpolarized rubidium on the wall of the cylinder will transfer energy and lose their alignment. The more rubidium on the wall, the more collisions and less time the atoms spend in the aligned state.

A process recommended by Precision Glassblowing of applying heat to the cell while keeping the stem cool allowed us to melt the rubidium and move it to the stem. We kept the stem cold by securing the stem in a cold, wet paper towel in a vice, then applied heat to the walls to direct the Rb atoms into the stem. However, it was important to ensure the heat applied did not exceed the melting point of paraffin in order to leave the wall coating intact.

After heat gunning our cell, visual improvements were noticed on the definition

of the reservoir in the stem (Fig 4.8(a)). NMOR results proved this successful as our NMOR feature width narrowed substantially. Fig. 4.7 compares widths before and after heat gunning the vapour cell. Fitting the data using Eq. 4.1, the corre-

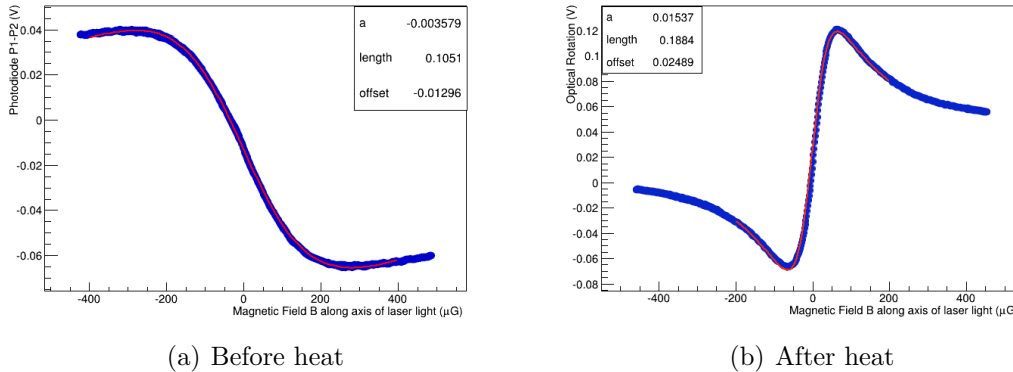


Figure 4.7: 4.7(a) shows a previous NMOR feature with a width of  $\sim 500 \mu\text{G}$ . 4.7(b) shows a clear improvement in signal and feature shape with a width of  $\sim 130 \mu\text{G}$ . Both data sets were fit to Eq. 4.1 The phase change of each feature is likely due to a 90 degree shift in half wave plate angle.

sponding  $a_{before} = 0.003579 \text{ 1}/\mu\text{G}$  and  $a_{after} = 0.01537 \text{ 1}/\mu\text{G}$  give NMOR widths of  $\sim 550 \mu\text{G}$  to  $\sim 130 \mu\text{G}$  that confirm substantial narrowing. This result motivated further investigation and study into a procedure to measured the relaxation rate  $\gamma_{rel}$  of cells.

## Relaxation Time

A system to measure  $\gamma_{rel}$  was built using [7] as a reference. The apparatus was built previous to the heat gunning of the cell so it was not possible to take a comparison measurement. Fig 4.8 displays our results. When the pump beam is blocked, a decaying exponential (Eq. 2.7) was fit to the data. This yielded a corresponding time constant of  $\gamma_{rel} = 484.4 \text{ s}^{-1}$ , where  $\tau_{rel} = 1/\gamma_{rel}$  and thus a  $\tau_{rel}$  of 2.1 ms. Compared to a Balabas cell with  $\tau_{rel}$  in seconds, our cell is incomparable in quality. An uncoated cell was also tested in our apparatus and the resulting

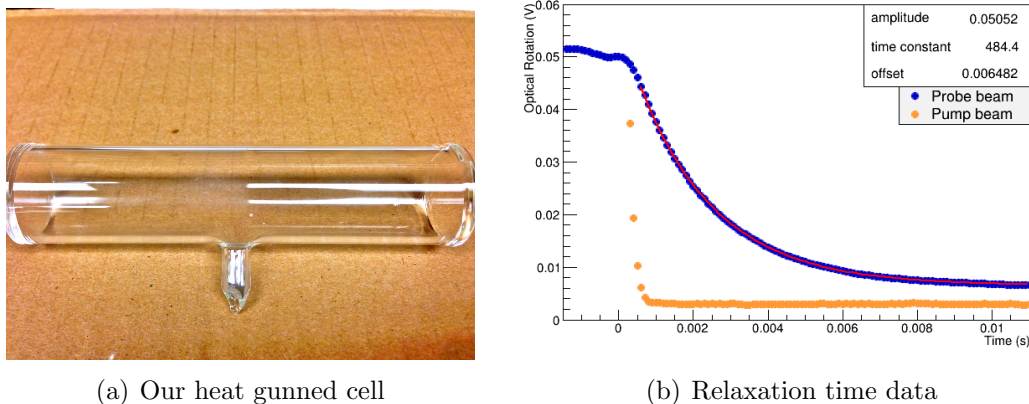


Figure 4.8: (a) Our cell after heat gunning. There is now a clear Rb deposit in the stem reservoir. (b) Measurement of optical rotation signal (blue) after blocking the pump beam (yellow) using our cell. Once the pump beam signal is fully off, optical rotation was fit to a decaying exponential to measure the relaxation time of cells where the time constant  $\tau_{rel} = 1/\gamma_{rel}$ .

data showed essentially zero relaxation time. This supports the use of coated cells versus uncoated cells.

Although we discovered a large narrowing after heat gunning our cell, the relaxation time is still extremely small relative to the cell used in Ref.[6]. As a result, cell quality is confirmed to be the primary limitation in improving our system in the future.

A cell received by D. Budker shows the stem reservoir system clearly with the bulk of the rubidium stored in the stem (Fig. 4.9).

The results shown in Fig. 2.3 are obtained using a cell similar to Fig. 4.9. Ideally, a cell of this quality will be purchased in the future for further study.

## 4.2 NMOR at Non Zero Field

The previous discussion involving NMOR has revolved around the system operating at zero field. In order for an all-optical atomic magnetometer to be practical, it must be able to operate at non zero magnetic fields as well. Achieving this re-

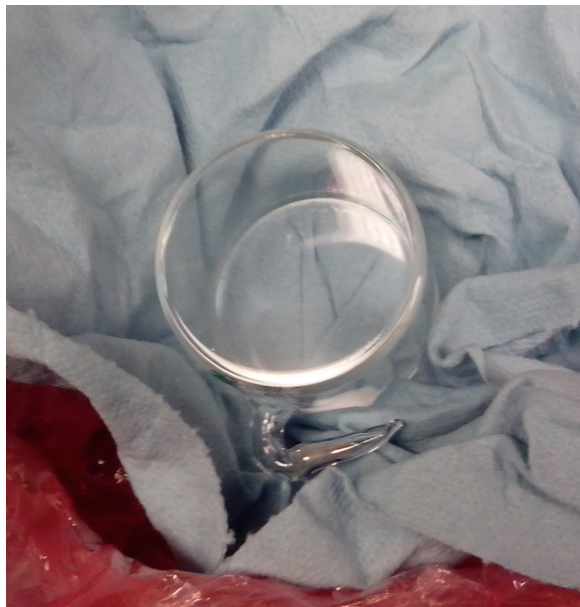
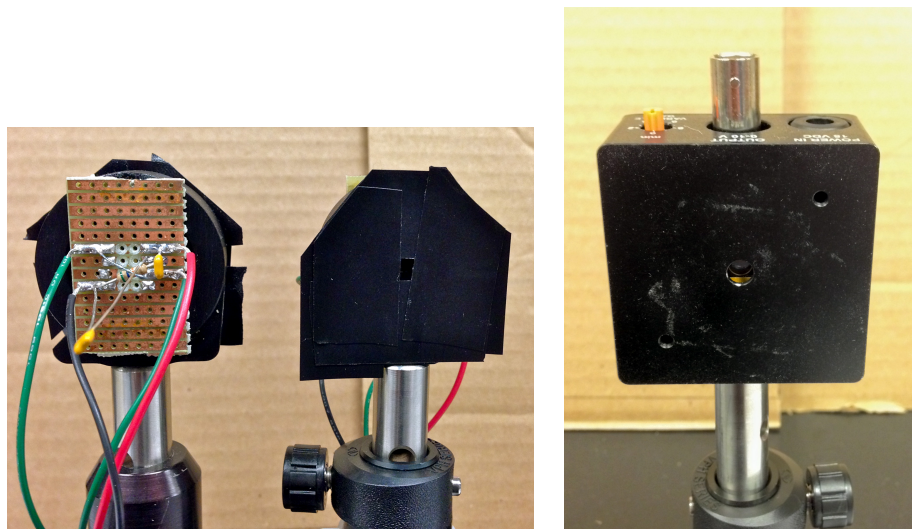


Figure 4.9: Paraffin coated rubidium vapour cell received by D. Budker. The stem below the cylinder is the reservoir and the grey colour is the rubidium stored within. The cell was not received in time for this thesis to test experimentally in our set up.

quires the pump light to be modulated at high frequencies ( $\sim 500$  kHz for Earth's field of 0.3 G). The nEDM experiment requires the magnetometer to operate at a field which corresponds to a modulation frequency of 20 kHz. Potential bandwidth limitations on our system were considered to be the AOM and the photodiode.

The AOM input and output holes are very small -  $< 2$  mm<sup>2</sup> - and must be hit directly to ensure proper modulation. Using two long focal length lenses on either side of the AOM, the large beam of 15 mm<sup>2</sup> was focused and aimed precisely through the crystal inside the AOM. This is supposed to be important for achieving higher bandwidth from the AOM [13].

Once we eliminated focusing into the AOM as a limitation, our attention turned to the photodiode. If the light would be modulated faster than the diode could respond, obvious problems would arise. The apparatus in Fig. 3.8 is designed to test the bandwidth of a single photodiode. Our initial photodiodes (Fig. 4.10(a)) were known to be low bandwidth ( $\sim 8$  kHz), but the extent of the limitations correlated to this were unknown.



(a) Monolithic photodiodes

(b) Hinds photodiode



(c) New Focus dual photodiode

Figure 4.10: (a) Bandwidth = 8 kHz (b) Bandwidth =  $>1$  MHz (gain dependent)  
 (c) Bandwidth  $>150$  kHz (gain dependent)

As we modulated the pump beam, we measured the response time of the photodiode. With the AOM modulated at 10 kHz, the resulting response time was greater than  $10 \mu\text{s}$  (Fig. 4.11(a)). We then substituted a Hinds photodiode (Fig. 4.10(b)) which has a higher bandwidth than previous. We were able to increase the modulation frequency drastically and at 100 kHz the response time was still less than a  $\mu\text{s}$  (Fig. 4.11(b)).

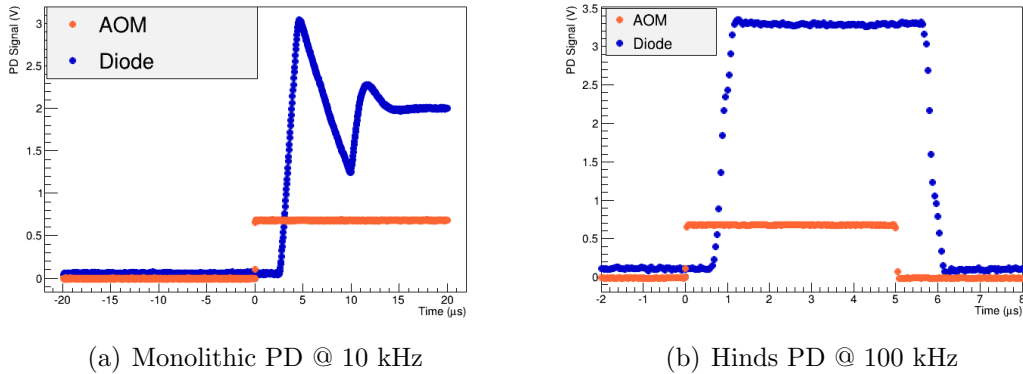


Figure 4.11: Response seen in photodiode for square-wave input to AOM. (a) Monolithic photodiode (Fig. 4.10(a)). Response time  $<10 \mu\text{s}$ . (b) Hinds photodiode (Fig. 4.10(b)). Response time  $<1 \mu\text{s}$ . Orange is AOM input signal and blue is the response from the photodiode. Time lag of  $<1 \mu\text{s}$ .

For this reason, we were able to quantitatively prove the limiting bandwidth of the AM NMOR system was in fact the photodiodes and not the AOM itself. We were able to operate our system at frequencies approaching 100 kHz with negligible response time. This motivated the purchase of the high bandwidth New Focus dual photodiode (Fig. 4.10(c)) used in the system for the remainder of this thesis as its response features and specifications are quite similar to the Hinds single photodiode.

### 4.3 Magnetometry

As stated previously, the intention of this research is to develop a magnetometer sensitive to field changes  $<1 \text{ nG}$ . By narrowing the NMOR width, the slope of optical rotation versus field at zero field increases and hence smaller changes in field can be more readily detected. In this experiment, we sought to modulate the magnetic field and see if we could see a change in the optical rotation signal ( $P_1 - P_2$ ).

The set up used is the same as for zero field NMOR in Fig. 3.1. To decrease the magnitude of field fluctuations, we added larger resistors in place of the variable

resistor into the coil schematic illustrated in Fig. 3.6. As the field fluctuates, the NMOR feature is noticeable and signifies the ability to detect magnetic fields to the magnitude of the applied field. An example of this is shown in Fig. 4.12.

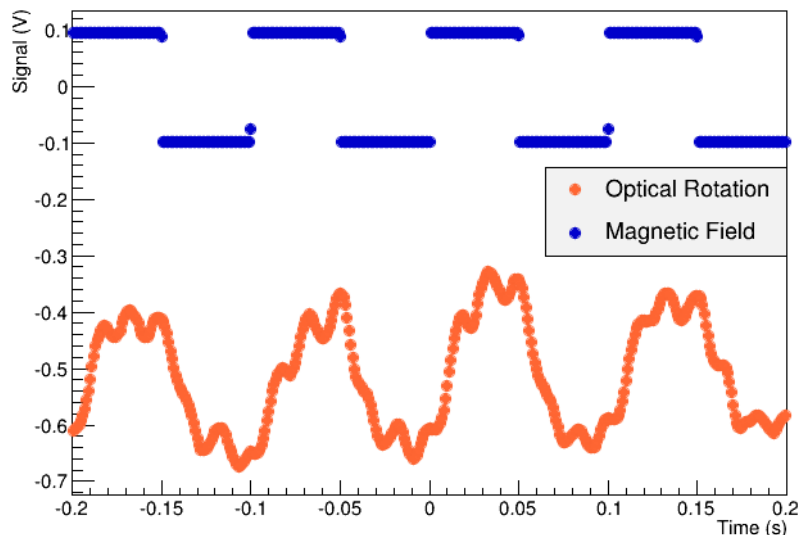


Figure 4.12: Optical rotation feature as the magnetic field is swept at 10 kHz about 48 nG. Variations in magnetic field are easily detected at this magnitude. 100 k $\Omega$  resistor used.

We continued to decrease the field until the feature was no longer detectable. At 25 nG, the feature was still noticeable (Fig. 4.13), but at 10 nG it was no longer possible to discern the signal from the noise (Fig. 4.14).

This system was extremely sensitive to 60 Hz noise from room lights and vibrations. To compensate, a high pass filter was inserted to filter out the noise in the photodiode signal. Although we have increased the sensitivity of our magnetometer by ten fold, there is still much needed improvement to reach the <1 nG nEDM target.

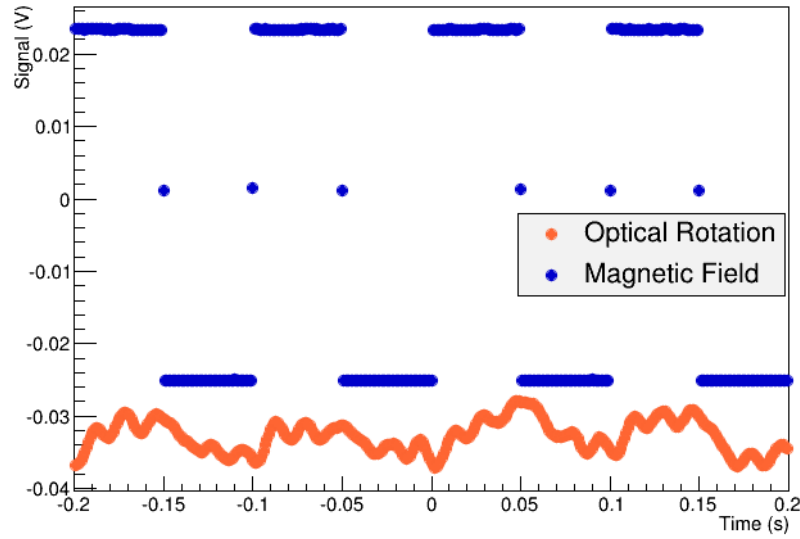


Figure 4.13: Optical rotation feature as the magnetic field is swept at 10 kHz about 25 nG. Variations in magnetic field are able to be detected at this magnitude. As the magnetic field changes, the optical rotation signal also changes. 1000 k $\Omega$  resistor used.

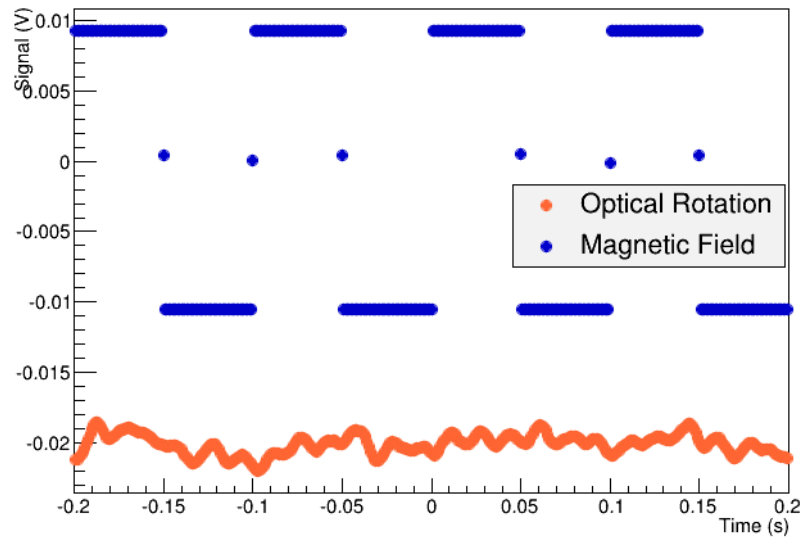


Figure 4.14: Optical rotation feature as the magnetic field is swept at 10 kHz about 10 nG. Variations in magnetic field are not able to be detected at this magnitude, thus limiting our sensitivity. 1000 k $\Omega$  resistor used.

# Chapter 5

## Results and Future Work

### 5.1 Results

Throughout the course of this thesis, we studied and improved many different aspects of the rubidium NMOR system. Magnetic fields are calibrated and well controlled both along and off the axis of laser light. New shielding reduces remnant fields at the cell to less than  $10\ \mu\text{G}$  while degaussing also proves important to reducing fields to less than  $1\ \mu\text{G}$ . By improving magnetic shielding, we were able to reduce our NMOR peak to peak separation width by a factor of two to a width of  $\sim 500\ \mu\text{G}$ . Off axis fields are also now able to be controlled to the  $3\ \mu\text{G}$  level. Further, the sweep rate of the magnetic field was found to have adverse effects on the NMOR feature at high frequencies. We used slower sweep rates of  $1\ \text{Hz}$  to avoid broadening the width and preserving symmetry between the up sweep and down sweep.

Our studies of laser parameters yielded power broadening at high powers and quality loss in signal at low powers. For best results, we typically used the  $/28$  neutral density filter to achieve a power of approximately  $38\ \mu\text{G}$  at the cell. We also quantified the frequency detune from resonance to achieve maximum optical rotation. With an arbitrary zero point set with respect to the fine structure of rubidium, we found a detune of  $0.3\ \text{GHz}$  was optimal.

By applying heat to our vapour cell, we were able to modify the rubidium and create a more well defined reservoir in the stem of the cell. This directly decreased the NMOR width to  $130 \mu\text{G}$  (Fig. 4.7(b)). This was the narrowest feature observed to date by our system. The narrowing directly motivated the set up of an apparatus used to measure the relaxation time of the cell and quantify the quality of our cell. Our current cell was measured to have a relaxation time  $\tau_{rel}$  of 2.1 ms. Compared to cells made by M. Balabas, relaxation times are of order seconds [7]. Hence, cell quality needs improvement for further narrowing of the feature.

Using AM NMOR, we were able to diminish the limitations on non zero magnetometry by using an AOM and a high bandwidth photodiode. We proved our system is capable of working up to frequencies of 100 kHz with little noise. Since the nEDM experiment requires frequencies of 20 kHz, we successfully eliminated the barrier to measure non zero magnetic fields using NMOR.

Finally, we were able use our system as a magnetometer and detect variations in magnetic field as small as 25 nG. This is a vast improvement relative to the start of this research, though sensitivity must still increase to the  $<1$  nG level for the nEDM experiment.

## 5.2 Future Work

Future work for this project include the development of a dichroic atomic laser locking system (DAVLL) [14], higher quality cells, non-zero field measurements over long periods of time, mapping, and operation sensing polarization of hyper polarized Xe. We expect higher quality cells made by M. Balabas will narrow the NMOR width substantially and increase the sensitivity range of our magnetometer. Testing the cell received by D. Budker will support the purchase of cells from M. Balabas.

The advantages of DAVLL allows for laser stability over extended periods of

time. This prevents laser drift and keeps the system optimally tuned for long term studies. Preventing laser drift is crucial to achieving a practical all-optical magnetometer.

Furthermore, operation over extended periods of time at non-zero fields are important for the nEDM experiment. DAVLL is also needed for this to prevent laser drift. Using the system to sense polarization of hyper polarized Xe is also a possibility which would prove the ability to sense extremely small changes in magnetic field.

# Bibliography

- [1] J. Higbie, E. Corsini, and D. Budker. *Robust, High-Speed, All-Optical Atomic Magnetometer* arXiv:physics/060904.1.
- [2] P. Ripka. *Advances in fluxgate sensors* Sensors and Actuators A 106, 8 (2003).
- [3] H. Dang, A. Maloof, M. Romalis. *Ultra-high sensitivity magnetic field and magnetization measurements with an atomic magnetometer* Appl. Phys. Lett. 97, 151110 (2010).
- [4] S. Groeger, G. Bison, J. Schenker, R. Wynands, and A. Weis. *A High-sensitivity laser-pumped  $M_x$  magnetometer* Eur. Phys. J. D 38, 239 (2006).
- [5] D. Budker, W. Gawlik, D. Kimball, S. Rochester, V. Yashchuk, and W. Weis. *Resonant nonlinear magneto-optical effects in atoms* Rev. Mod. Phys. 74, 4, (2002).
- [6] D. Budker, V. Yashchuk, and M. Zolotarev. *Nonlinear Magneto-Optic Effects with Ultranarrow Widths* Phys. Rev. Lett. 81, 5788 (1998).
- [7] M. Graf, D. Kimball, S. Rochester, K. Kerner, C. Wong, D. Budker, E. Alexandrov, M. Balabas, V. Yashchuk. *Relaxation of Atomic Polarization in Paraffin-coated caesium vapour cells* Phys. Rev. Lett. 72, 023401 (2005).
- [8] D. Budker, D. Orlando, and V. Yashchuk. *Nonlinear Laser Spectroscopy and Magneto-optics* Am. J. Phys. 67, 584 (1999).

- [9] D. Kimball slides, *Non-Linear Magneto-Optical Rotation with Frequency-Modulated Light 2013*. [http://budker.berkeley.edu/D\\_Kimball\\_Qual/](http://budker.berkeley.edu/D_Kimball_Qual/).
- [10] D. Steck, *Rubidium 85 D Line Data*. <http://steck.us/alkalidata>.
- [11] R. Alexandrov, M. Balabas, D. Budker, D. English, D. Kimball, C. Li, and V. Yashchuk. *Light-induced desorption of alkali atoms from paraffin coating*. Phys. Rev. A 66, 042903 (2002).
- [12] M. Momeen, G. Rangarajan, and V. Natarajan. *Transient response of non-linear magneto-optic rotation in a paraffin-coated Rb vapour cell*, Phys. Rev. Lett. 81, 013413, (2010).
- [13] T. Momose, private communication.
- [14] V. Yashchuk, D. Budker, and J. Davis. *Laser frequency stabilization using linear magneto-optics* Rev. Sci. Instrum. 71, 341 (2000).